JOURNAL OF MATERIALS SCIENCE **35** (2000) 1759–1771

Inhibition of chloride pitting corrosion of Zircaloy-4 alloy in highly radioactive water by radiolytic nitrate and hydrogen peroxide

G. BELLANGER*
Department Tritium-137, Commissariat à l'Energie Atomique, Centre d'Etudes de Valduc, F21120, Is sur Tille, France
E-mail: Gilbert.Bellanger@wanadoo.fr

J. J. RAMEAU
Laboratoire d'Electrochimie et de Physicochimie des Matériaux et des Interfaces, Ecole Nationale Supérieure d'Electrochimie et d'Electrométallurgie, Institut National Polytechnique de Grenoble, Domaine Universitaire, B.P. 75, F38402, Saint Martin d'Hères, France

We report an investigation of the pitting corrosion susceptibility of Zircaloy-4 alloy in presence of radiolytic chloride, nitrate and hydrogen peroxide. The electrochemical behavior of Zircaloy-4 was essentially studied using cyclic voltammetry and electrochemical impedance spectroscopy to provide an indication of mechanisms and oxide layer modifications. The experiments have shown that the pitting corrosion behavior is dependent on the concentration of these radiolytic species in tritiated water. Nitrate shows pronounced inhibitory action due to adsorption of the ammoniac formed on the passive oxide layer buffering the pH, which stops pit initiation and assists repassivation of the oxide surface. The presence of both hydrogen peroxide and NO_3^- produces other effects. The passive oxide layer is thicker and its characteristics change in the bulk. Also, pit initiation is stopped whereas it is more difficult to obtain repassivation of existing pits. This can be explained by the capability of $^3H_2O_2$ to oxidize the surface and thus enhance passive oxide formation. But, in this case, $NO_3^-/N^3H_4^+$ adsorption should be hindered by the $^3H_2O_2$ present and consequently there is less buffering of the surface pH limiting repassivation of the existing pits. However, with these two combined effects: pH kept constant on the Zircaloy-4 surface and enhancement of the oxide layer intrinsic characteristics, less pitting is observed than in presence of chloride ions alone.

1. Introduction

In this work, the passivity and pitting aspects of Zircaloy-4 with respect to its application in nuclear reprocessing installations were studied using radioactive aqueous solutions. The specific case involved here is tritiated water which is an internal β^- radiation source. Tritium decays with the emission of a β^- particle and a γ_e antineutrino in tritiated water. The energy released decomposes water molecules along the path of the particle. Effects of β^- particle energy and radiolytic products due to tritium were recently published by our laboratories for other alloys [1–6]. The reaction occurring in this decay is:

$$^3H_2O \rightarrow 2^3He + O^\bullet + 2\beta^- + \gamma_e \quad E_{max} = 18.6 \times 2\,keV \tag{1}$$

The tritiated water molecules are ionized leading to the chemical reaction stage. The overall radiolytic reaction is:

$$2^3H_2O + \beta^- \rightarrow {}^3H^\bullet,$$
$$^3HO_2^-, {}^3HO_2 \ldots \leftrightarrow {}^3H_2O_2 + {}^3H_2 \tag{2}$$

This reaction leads to the formation of tritiated hydrogen peroxide. The pK (equilibrium constant) for $^3H_2O_2$ and $^3HO_2^-$ is 12 as shown in [7]. Therefore, in the present study, realized at neutral pH, it can be expected that the electroactive form does not predominate.

Relatively concentrated solutions of nitrate are produced in tritiated water reprocessing installations. This can be explained by the effect of β^- particles on

* Author to whom all correspondence should be addressed.

nitrogen in the air used for gaseous tritium oxidation. The reactions are from Refs [8–10]:

$$N_2 + \beta^- \rightarrow 2N^\bullet \quad (3)$$

$$N^\bullet + 4^3HO_2^- \rightarrow NO_3^- + 2^3H_2O + 3O^\bullet \quad (4)$$

The presence of chloride is explained by the fact that tritium in tritiated water is easily taken up (∼3%) in organic polymers by chemical bonds, e.g., $(–R–^3H, Cl–)_n$. As with water, the β^- particle energy decomposes organic polymers. The decomposition reaction for the polyvinyl chains is:

$$(–R–^3H, Cl–)_n + \beta^- \rightarrow \left(–R'–^3H_2–\right)n' + nCl^- \quad (5)$$

Similarly, the formation of ammoniac from breaking the polyimine chain bonds with β^- radiation is observed. Mass spectrometric analysis of the gases shows a significant concentration of this species.

$$\left(\begin{matrix}^3H\\R\end{matrix}\!\!>\!C{=}N–\right)_n + 2(n' + 2n)^3H^\bullet + n^3H_2O + \beta^- \rightarrow \left(–R'–^3H_2–\right)_{n'} + n N^3H_4O^3H + nC^3H_4 \quad (6)$$

The choice of Zircaloy-4 as alloy in the nuclear plants is justified by all the qualities of its passive layer. Oxidation of Zircaloy under electrochemical conditions has received a great deal of attention [11–15]. It is well known that its corrosion resistance is due to the protective capacity of its passive oxide layer but unfortunately with chloride and powerful oxidants, local depassivation by cracking of oxide layers can occur, leading to pitting. However, nitrates act as inhibitors. We have found nothing in the literature for a mixture of these three species. For these different reasons, the behavior of Zircaloy-4 was studied using tritiated water containing chloride, nitrate and hydrogen peroxide over a wide range of passive potentials.

2. Experimental equipment and procedure

The tritium concentration in tritiated water was determined using a Cetaram microcalorimeter. To suppress any uncertainties, the experiments were carried out at the same tritium concentration (16% ^3H_2O) to ensure that there was no variation in the amount of radiation energy arriving at the oxide layer. In each corrosion test, tritiated hydrogen peroxide was analyzed by potentiometry and the desired concentrations were obtained by electrolytic reduction. The chloride and nitrate concentrations were measured with specific electrodes in order to determine their effects on the behavior of the Zircaloy-4.

The measurement sequence for electrochemical impedance spectroscopy in passivity was: (1) to apply a given potential, E, to achieve the stationary current before obtaining the impedance spectrum, (2) to shift the potential in a positive direction up to $E + \Delta E$, then to obtain the impedance spectrum with good reproducibility at this new potential, (3) to repeat the sequence from point 2 in the potential range. Applying this procedure, it is possible to demonstrate oxide thickening. The Circelec computer program written by Diard *et al*. [16, 17] was used to interpret the experimental impedance diagrams to obtain values of the electrochemical components. The working electrode was a Zircaloy-4 rod embedded in a Teflon holder. The reference and auxiliary electrodes were, respectively, saturated calomel (SCE) and platinum electrodes. Prior to use, the working electrode was mechanically polished using 1000 mesh grade silicon carbide sheets, then with diamond paste down to 1 μm.

TABLE I Chemical composition of Zircaloy-4

Elements	Sn	Fe	Cr	O	Zr
Weight%	1.45	0.21	0.10	0.01	bal.

The composition of the Zircaloy-4 is given in Table I. The used zircaloy sample was processed by hot rolling followed by recrystallization annealing for 2 hours at 650°C under vacuum. Its surface was examined with a scanning electron microscope and it was found that the alloy sample is characterized by an equiaxial grain size of 25 μm diameter.

3. Experimental results

Before discussing the shape of these curves and their interpretation we must provide details of the development of the experimental study. Initially, we describe the overall effect on the polarization curves when Cl^-, NO_3^- and $^3H_2O_2$ are present together. Next, using voltammetry or electrochemical impedance spectroscopy, we study each of these species alone or in groups of two or three to show the individual and reciprocal influence on pitting corrosion and passivity phenomena.

3.1. Anodic polarization curves

In the polarization curves (Fig. 1), the passive currents are higher with increasing $^3H_2O_2$. The corrosion potential does not change with $^3H_2O_2$ presence. In the transpassivity, it is observed that the repassive potential decreases whereas the pitting potential increases and the pitting current increases with $^3H_2O_2$.

3.1.1. Analysis and interpretation of polarization curves

The interpretation for higher passive currents could be that $^3H_2O_2$ thickens the oxide layer forming constraints. At more negative potentials than the corrosion potential, the current should correspond to the $^3H_2O_2$ reduction with formation of O^3H^-. It can be seen that $^3H_2O_2$ reduction is not really involved. This results from the ZrO_2 layer which is already present and partially inhibits $^3H_2O_2$ reduction by greatly limiting the passage of current in the oxide, which behaves as an insulating capacitance. The ZrO_2 presence at these

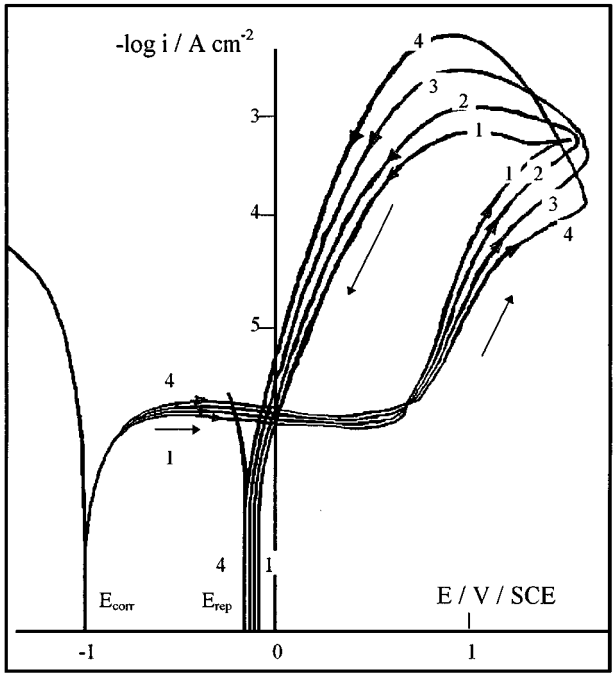

Figure 1 Polarization curves with chloride, nitrate and hydrogen peroxide. v: 5 mV s^{-1}, A: 0.2 cm^2, pH 6, 0.1 mol dm^{-3} Cl^-, 0.1 mol dm^{-3} NO_3^-, 1: 3×10^{-2}, 2: 5×10^{-2}, 3: 7×10^{-2}, 4: 0.1 mol dm^{-3} $^3H_2O_2$.

negative potentials is shown in the Pourbaix electrochemical equilibrium diagram [18] for zirconium. The corrosion resistance results from its strong affinity for oxygen resulting in the formation of a thin protective layer of oxide spontaneously formed at the lower potentials. Nevertheless, oxidation of Zircaloy-4 continues to occur by the following anodic and cathodic reactions throughout the passive oxide layer with a very low oxidation current of a few μA cm^{-2}. To simplify, Zircaloy-4 is represented by the symbol for zirconium.

Cathodic sites:

$$^3H_2O + e^- \rightarrow O^3H^- + {}^3H \qquad (7)$$

$$^3H_2O_2 + 2e^- \rightarrow 2\,O^3H^- \qquad (8)$$

The cathodic currents in the above reactions are:

$$i_{c_1} = -2k_{c_1}F[^3H_2O]^{\nu\text{red}} \exp\frac{-eE}{kT} \qquad (9)$$

$$i_{c_2} = -2k_{c_2}F[^3H_2O_2]^{\nu\text{red}} \exp\frac{-eE}{kT} \qquad (10)$$

Anodic sites leading to passive oxide layer thickening:

$$Zr + 2\,^3H_2O \rightarrow ZrO_2 + 4\,^3H^+ + 4e^- \qquad (11)$$

As above, the anodic current is:

$$i_a = 4k_aF\left[^3H_2O\right]^{\nu\text{ox}} \exp\frac{2eE}{kT} \qquad (12)$$

In Equations 9, 10 and 12, the different k_{a,c_n} are the anodic and cathodic reaction rate constants, k the Boltzmann constant, e the charge of the electron, ν the electrochemical reaction orders and E the applied potential. From these equations, acidification and alkalization occur at the surface which can locally modify the pH (Equations 7, 8, 11). In fact, nitrate should act to keep the surface pH buffered by means of chemisorbed $N^3H_4^+$ film formation. Also, it will be shown later that oxide formed with NO_3^- present is definitely more protective than that formed in its absence, or in its presence with that of $^3H_2O_2$. $^3H_2O_2$ should certainly be responsible for removal of an adsorbed $N^3H_4^+$ film leading to a repassive potential shift in the negative direction. According to Fig. 1, the oxide layer formed under these conditions is associated with localized corrosion by Cl^-, and has been identified as participating in protection depending on all the radiolytic species present. The result is that, for this medium, the properties and composition of the oxide should be different from those obtained in the absence of $^3H_2O_2$ and NO_3^-.

3.2. Voltammetric curves

The use of relatively fast scan rates is unusual in corrosion testing, and the justification for this technique is given by Morris and Scarberry [19] and Darowicki and Krakowiak [20]. With the rapid-scan voltammograms, we expect to find more easily the variation of pitting and repassivation potentials and the maximum current in pitting, first with only chlorides (Fig. 2) then, with both chloride and nitrate (Fig. 3) and finally with different $^3H_2O_2$ concentrations and with NO_3^- and chlorides (Fig. 4). In these figures, the "pseudo" active peak of a few μA indicates oxide rearrangement by thickening according to Equation 11.

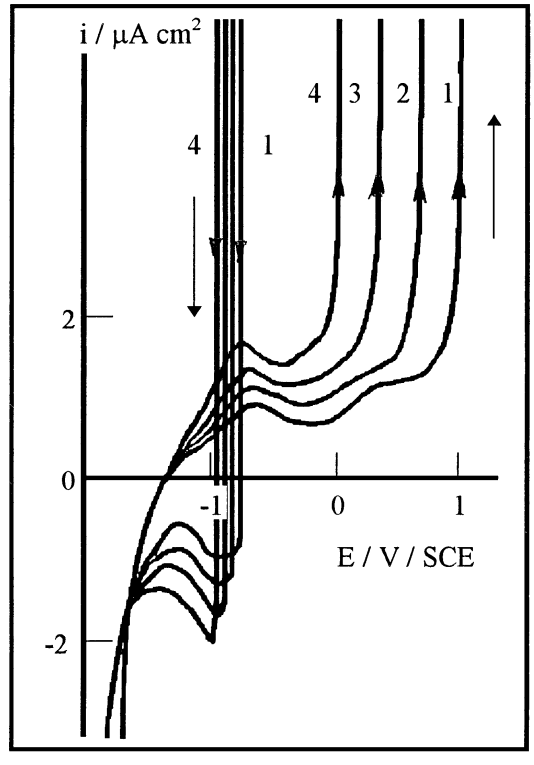

Figure 2 Voltammetric curves with chloride alone. v: 200 mV s^{-1}, A: 0.2 cm^2, pH 6, 1: 4×10^{-2}, 2: 6×10^{-2}, 3: 8×10^{-2}, 4: 0.1 mol dm^{-3} Cl^-.

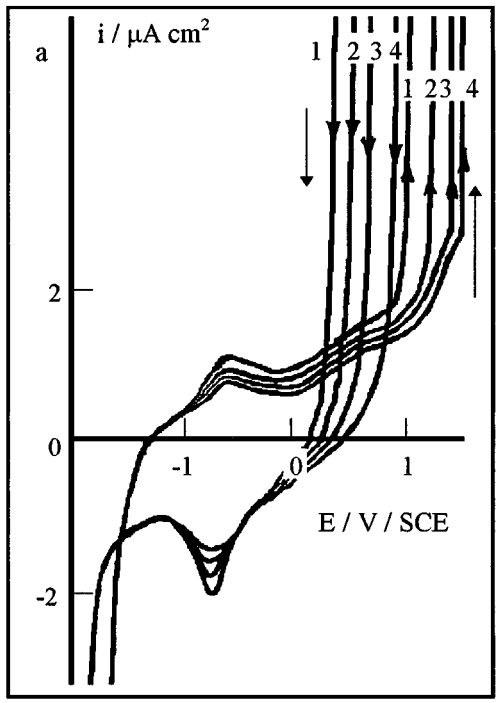

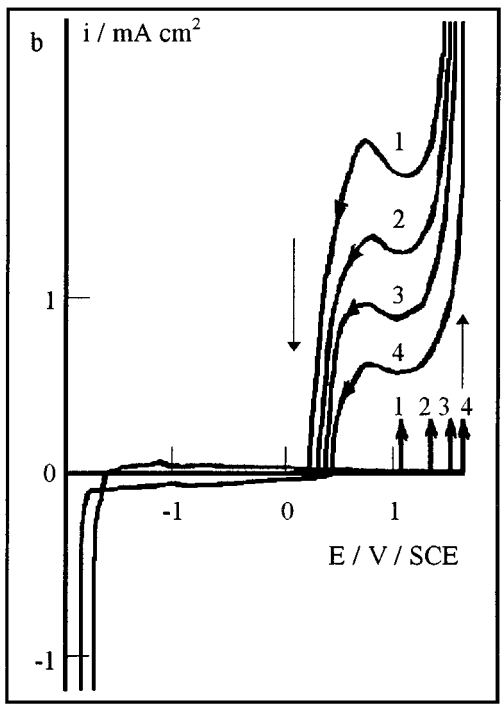

Figure 3 Voltammetric curves with chloride, nitrate and without hydrogen peroxide, a: expanded current scale, b: higher current scale. v: 200 mV s^{-1}, A: 0.2 cm^2, pH 6, 0.1 mol dm^{-3} Cl^-, 1: 3×10^{-2}, 2: 5×10^{-2}, 3: 7×10^{-2}, 4: 0.1 mol dm^{-3} NO_3^-.

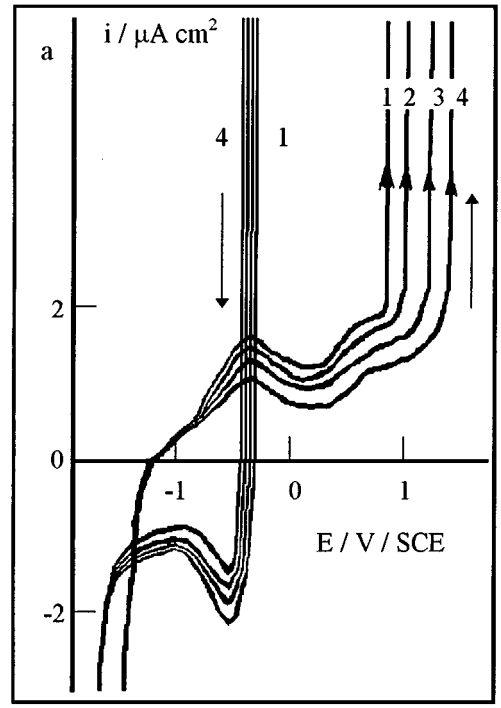

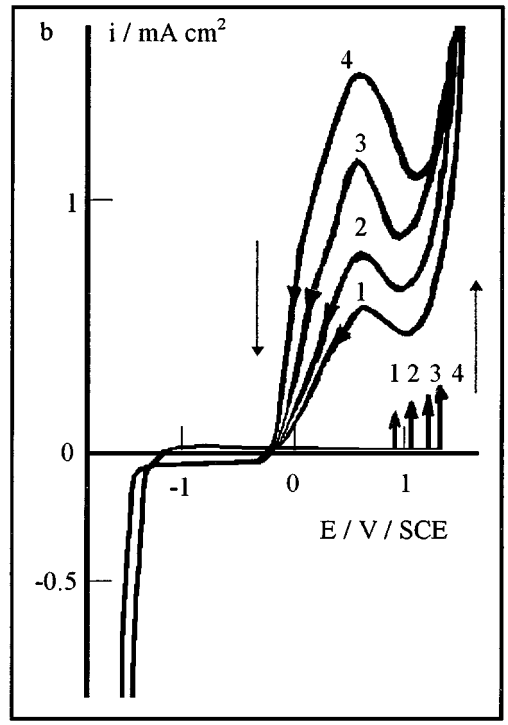

Figure 4 Voltammetric curves with hydrogen peroxide, nitrate and chloride, a: expanded current scale, b: higher current scale. v: 200 mV s^{-1}, A: 0.2 cm^2, pH 6, 0.1 mol dm^{-3} Cl^-, 3×10^{-2} mol dm^{-3} NO_3^-, 1: 3×10^{-2}, 2: 5×10^{-2}, 3: 7×10^{-2}, 4: 0.1 mol dm^{-3} $^3H_2O_2$.

3.2.1. Analysis of voltammograms obtained with Cl^-

In the passive domain (Fig. 2), the anodic current increases slightly, signifying a mismatch with Cl^-. Nevertheless, the passive current before pitting is very low. The passive potential range is smaller at higher Cl^- concentrations. In the transpassive-passive region, the pitting and repassive potentials shift dramatically toward smaller values with higher Cl^- concentration. The interpretation is that the pit propagation and pitting increase with chloride present. In fact, Energy dispersive X-ray analysis reveals the presence of Cl in the passive oxide layer (Fig. 5) for the sample used in voltammograms after a cleaning procedure. Also, chloride crosses the oxide layer by diffusion.

3.2.2. Analysis of voltammograms obtained with NO_3^- and with Cl^-

In Fig. 3, the passive potential range is wider with NO_3^- present. In the transpassive region, the maximum pitting current decreases and the pitting and repassive

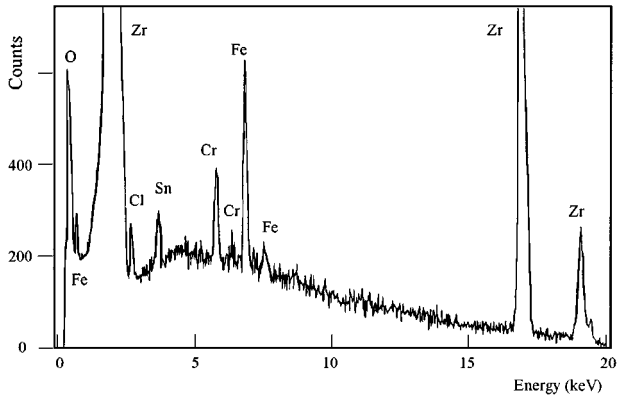

Figure 5 Energy Dispersive X-Ray analysis examinations. Peaks of elements in Zircaloy-4 and peak of Cl showing its presence in the oxide (sample of Fig. 2).

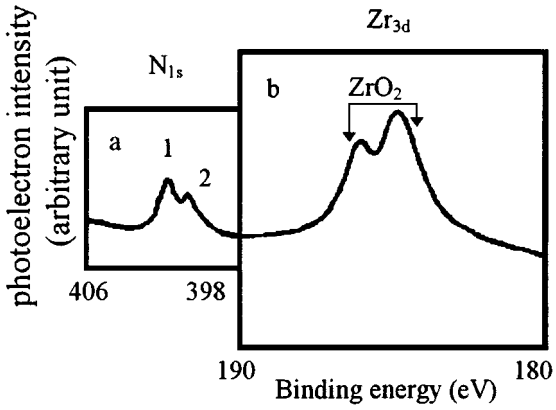

Figure 6 X-Ray Photoelectron Spectroscopy of Zircaloy-4 after passivation showing presence of $N^3H_4^+$ on the oxide. a: XPS spectrum of N_{1s} peak, 1: $N^3H_4^+$, 2: N^3H_3, b: XPS spectrum of Zr_{3d} peak.

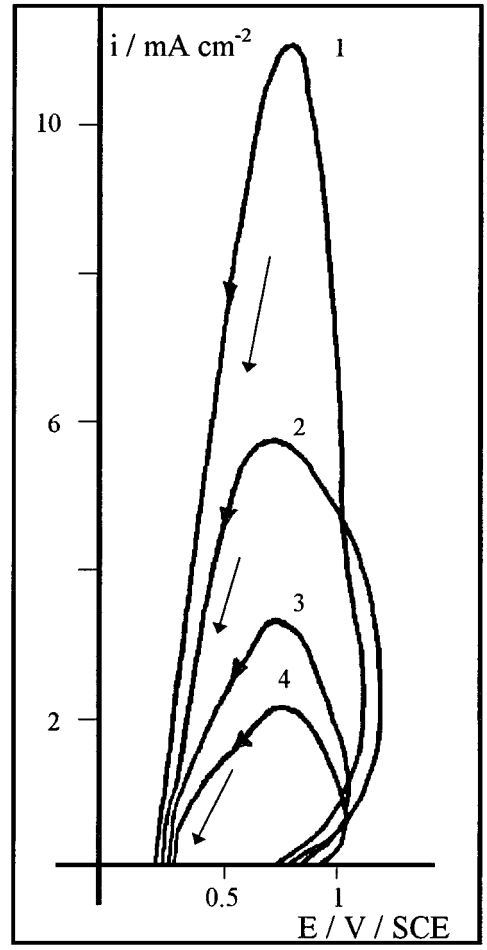

Figure 7 Voltammetric curves realized for different scan rates and with chloride and nitrate present. *A*: 0.2 cm^2, pH 6, 0.1 mol dm^{-3} Cl^-, 0.1 mol dm^{-3} NO_3^-, *v*: 1: 25, 2: 50, 3: 100, 4: 200 mV s^{-1}.

potentials shift toward higher values with increasing NO_3^- concentration. Evidently, the oxide layer is clearly more protective, and in this case pitting is more difficult to obtain, as observed by Clayton and Olefjord [21, 22]. To investigate the nature of the passive layer formed under these conditions on the Zircaloy-4 surface, the oxide surface was analyzed by X-ray photoelectron spectroscopy (Fig. 6) and a small peak is observed at 400 eV indicating the presence of N. The peak suggests effectively that NO_3^- is reduced to $N^3H_4^+$. This would indicate that $N^3H_4^+$ is present as adsorbate on the surface. $N^3H_4^+$ acts to keep the buffered surface pH constant and to retain passivity and delay pitting nucleation. This indicates that the pitting corrosion rate and passivity are dependent on the absence of any superficial pH modification towards acid pH in pits. Chloride ions are less adsorbed and require more time to cross the passive oxide layer under these conditions as seen, e.g., in Fig. 7 where an increase in the scan rate leads to decreasing the pitting currents. These results show, without any doubt, the effectiveness of NO_3^- as corrosion inhibitor in pitting initiation.

3.2.3. Analysis of voltammograms obtained with $^3H_2O_2$, NO_3^- and Cl^-

The corrosion potential does not change (Fig. 4) when the $^3H_2O_2$ increases. This behavior results from the difficulty of $^3H_2O_2$ reduction whose current is superimposed on the passivation current. In the passive domain, the anodic current is slightly higher than that obtained in Section 3.2.2 signifying a greater thickness and a risk of more defective oxide. The passive potential range is larger when $^3H_2O_2$ concentration increases. In the transpassive-passive region, the pitting potential shifts toward higher values, whereas the repassive potential shifts slightly toward smaller values and the maximum pitting current increases when $^3H_2O_2$ concentration increases. This can be explained by the fact that the $^3H_2O_2$, as a powerful oxidizing species, is capable of oxidizing the surface and limits pit initiation whereas it makes more difficult repassivation of existing pits.

3.2.4. Results and discussion

This discussion makes use of Aramaki *et al.* [23], Al-Kharafi [24] and Ming-Yu Chang and Ge-Ping Yu's remarks [25] on other metals and environments.

Influence on pitting potential Fig. 8 shows the linear variation of pitting potential, E_{pit}, as a function of the logarithm of the inhibitor to chloride concentration ratio. The pitting potential obtained with only chloride

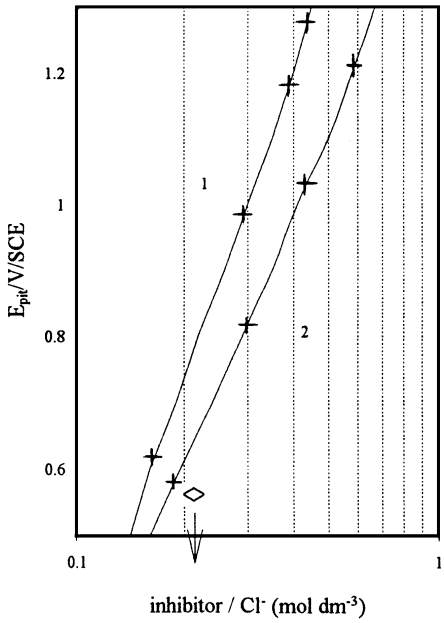

Figure 8 Pitting potential as a function of inhibitor concentration. 1: 0.1 mol dm^{-3} Cl^-, variation of NO_3^- concentration according to Fig. 3 2: 0.1 mol dm^{-3} Cl^-, 3×10^{-2} mol dm^{-3} NO_3^-, variation of $^3H_2O_2$ concentration according to Fig. 4, ◇: Cl^- without inhibitor (arrow).

ions (E^0_{pit}) is represented by a diamond. In this figure, the pitting potential shifts towards higher values when the inhibitor-chloride ratio increases. This signifies that addition of inhibitor stops pit initiation for potentials under the curves as shown by analyzing the local currents (Fig. 9, plates a and b). Effectively, in plate b obtained at 0.8 V/SCE and for $NO_3^-/Cl^- = 0.35$, the studied section shows a greater area of zero local current indicating a marked tendency to limit pitting initiation sites. Also, pit initiation is less easily stopped by nitrate and $^3H_2O_2$ as seen in Fig. 8. Because these inhibitors provide a more perfect passive layer in the potential region under the straight lines, defects at the passive surface are repassivated.

Influence on repassivation potential The values of the repassivation potential, E_{rep}, as a function of the logarithm of the inhibitor to chloride concentration ratio are shown in Fig. 10. In this figure, the repassivity potential obtained with only chloride ions (E^0_{rep}) is represented by a diamond. Because NO_3^-, in the absence of $^3H_2O_2$, makes E_{rep} more positive, it is an effective inhibitor for establishing repassivation. NO_3^- plugs the pits by buffering the pH, as shown by Refaey and Rehim [26]. Nevertheless propagation of existing pits appears to occur at the lower concentration of inhibitors as suggested by the i_{max} values between E_{pit} and E_{rep} in the voltammograms (Figs 3b and 4b). The curve (Fig. 10) obtained with NO_3^- and $^3H_2O_2$ present shows a negative slope when hydrogen peroxide concentration increases. Localized corrosion is aided between E_{pit} and E_{rep} within the existing pits by $^3H_2O_2$ addition, and there is less repassivation than with NO_3^- alone. Thus, the inhibitive effects depend really on the inhibitor nature, concentration and potentials.

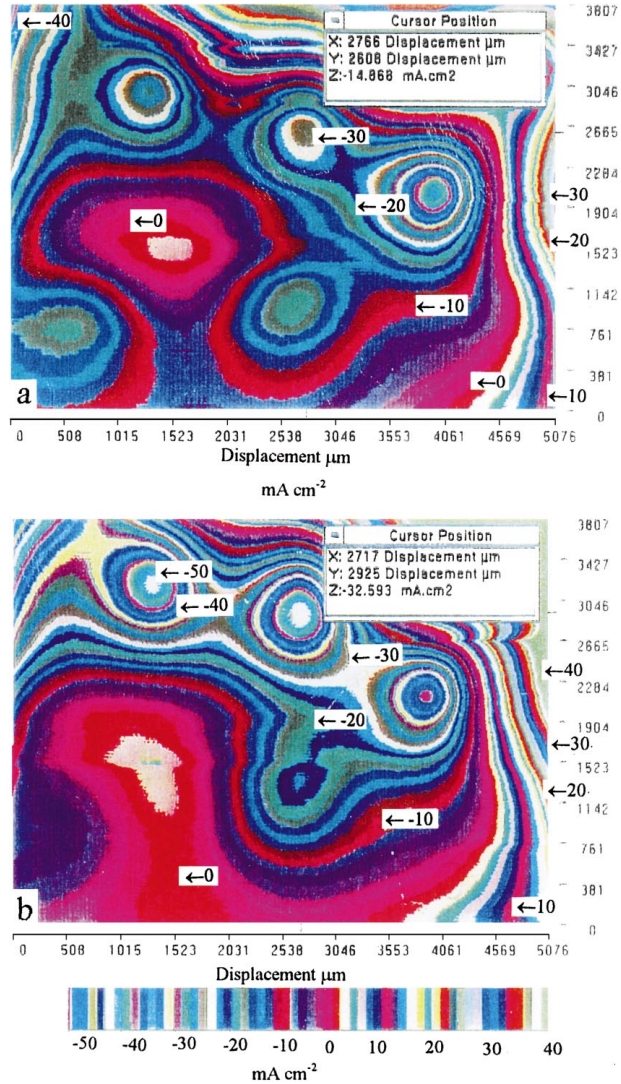

Figure 9 Photograph obtained by the Scanning Reference Electrode Technique. a: pitting micro-cells induced by Cl^-, b: local repassivation of pitting micro-cell induced by NO_3^-.

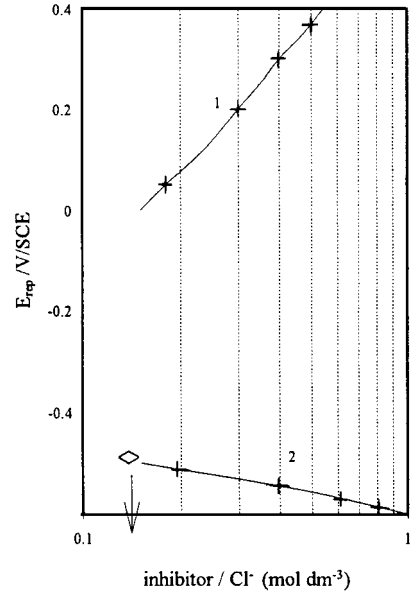

Figure 10 Repassivation potential as a function of inhibitor concentration 1: 0.1 mol dm^{-3} Cl^-, variation of NO_3^- concentration according to Fig. 3. 2: 0.1 mol dm^{-3} Cl^-, 3×10^{-2} mol dm^{-3} NO_3^-, variation of $^3H_2O_2$ concentration according to Fig. 4, ◇: Cl^- without inhibitor (arrow).

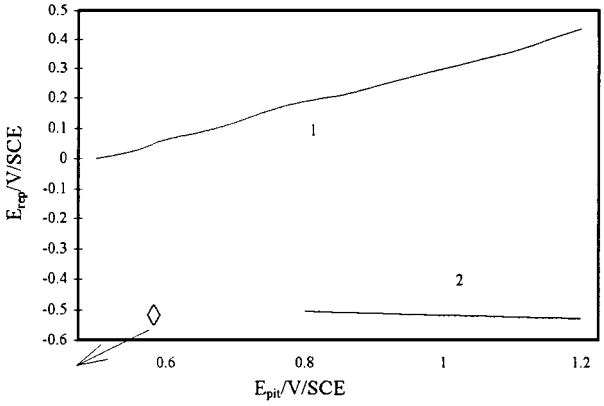

Figure 11 Relationship between E_{pit} and E_{rep}. 1: Cl^- and NO_3^-, 2: Cl^-, NO_3^- and $^3H_2O_2$, graph plotted according to Figs 8 and 10, ◇: Cl^- without inhibitor (arrow).

Influence on the gap between pitting potential and repassivation potential The graph giving the relationship between E_{pit} and E_{rep} is in Fig. 11. Two linear curves are obtained: one for NO_3^- with a positive slope, the other for NO_3^- with $^3H_2O_2$ where the slope is slightly negative. Each curve divides the figure into two domains: aggressiveness for points above the considered curve and inhibition below this curve. The NO_3^- inhibitor shifts both E_{pit} and E_{rep} in the positive direction, indicating suppression of both pit nucleation and initiation and slowing propagation of existing pits between E_{pit} and E_{rep}. On the other hand, NO_3^- with $^3H_2O_2$ changes E_{pit} towards a positive potential but E_{rep} shifts slightly towards a negative potential with increasing $^3H_2O_2$ concentration. It is definitely concluded that with $^3H_2O_2$ addition, the propagation of existing pits should be faster than for NO_3^- alone. Nevertheless, NO_3^- and $^3H_2O_2$ result in better repassivation than that for tritiated water containing only chlorides.

Influence on maximum current Without these inhibitors, it was observed that the pitting current reaches the higher maximum value (i^0_{max}), as represented by the diamond in Fig. 12. On addition of NO_3^-, the maximum current decreases indicating a significant limitation of the propagation of existing pits. Fig. 12 also shows higher values of i_{max} for $^3H_2O_2$ addition as compared with only NO_3^-. $N^3H_4^+$ adsorption should be hindered by $^3H_2O_2$ present and consequently there is less buffering of the surface pH limiting repassivation of the existing pits. As well, a thicker oxide layer, due to $^3H_2O_2$, should limit the pitting current. From these different curves, it appears that propagation of existing pits and the area corroded by pitting can be essentially avoided at higher NO_3^- concentrations.

Relation between the gap between E_{pit} and E_{rep} and maximum current In the potentials between E_{rep} and E_{pit} (ΔE), the inhibitors suppress pit nucleation by repairing defects in the passive layer. As a result, the potential difference $\Delta E = E_{pit} - E_{rep}$ can be associated

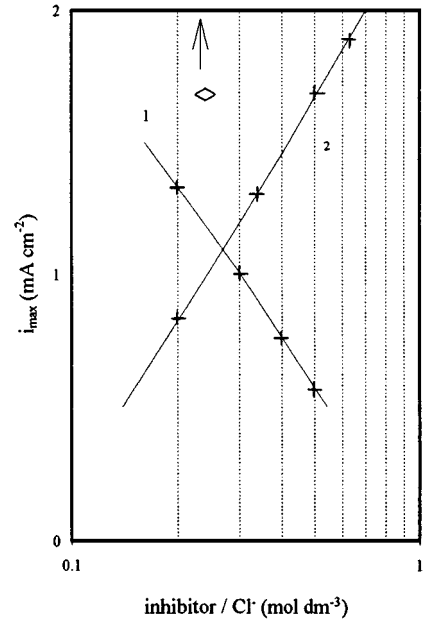

Figure 12 Maximum pitting current as a function of inhibitor concentration. 1: 0.1 mol dm^{-3} Cl^-, variation of NO_3^- concentration according to Fig. 3. 2: 0.1 mol dm^{-3} Cl^-, 0.1 mol dm^{-3} NO_3^-, variation of $^3H_2O_2$ concentration according to Fig. 4, ◇: Cl^- without inhibitor (arrow).

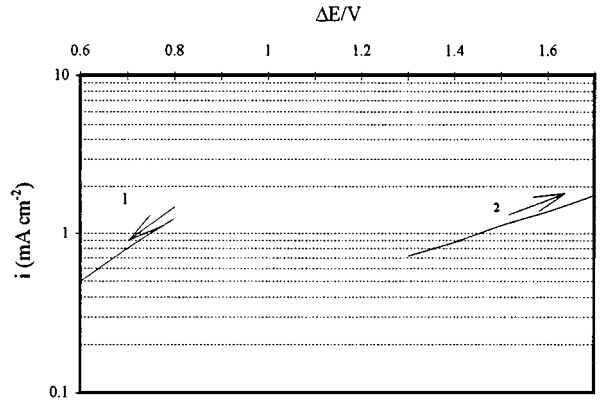

Figure 13 Relationship between the maximum pitting current and $\Delta E = (E_{pit} - E_{rep})$. 1: Cl^- and NO_3^-, 2: Cl^-, NO_3^- and $^3H_2O_2$, graph plotted according to Figs 8, 10 and 12, arrows: increasing ratio between inhibitor and chloride.

with a remarkable lowering of pitting current (i_{max}) as seen in Fig. 13 responding to Equation 13:

$$\log i_{max} = k_d \Delta E + k_e \qquad (13)$$

The values of $\log i_{max}$ for the plots of NO_3^- are to some extent lower than that obtained with $^3H_2O_2$ indicating inhibiting effects of NO_3^-. Hence, NO_3^- suppresses pit nucleation and slows the propagation of existing pits. Since with $^3H_2O_2$ addition, ΔE increases with i_{max}, in this case, it is difficult to have appreciable repassivation of the existing pits. These results confirm the previous conclusions: inhibition, nucleation or stimulation of pit formation and propagation of existing pits. Partial inhibition of existing pits is attributed to the presence of the inhibitor NO_3^-. In presence of $^3H_2O_2$, propagation of existing pits is not stopped leading to slowing down the repassivation. The presence of $^3H_2O_2$ has provided a partly beneficial effect on the inhibiting action of NO_3^-.

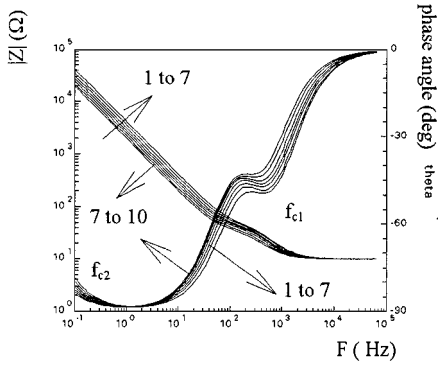

Figure 14 Experimental Bode spectra in presence of Cl^- in passivity. *A*: 0.2 cm^2, pH 6, 0.1 mol dm^{-3} Cl^-, 1: −1 V, 2: −0.97 V, 3: −0.95 V, 4: −0.92 V, 5: −0.9 V, 6: −0.87 V, 7: −0.85 V, 8: −0.82 V, 9: −0.8, 10: −0.77 V/SCE, parameter values in Table II.

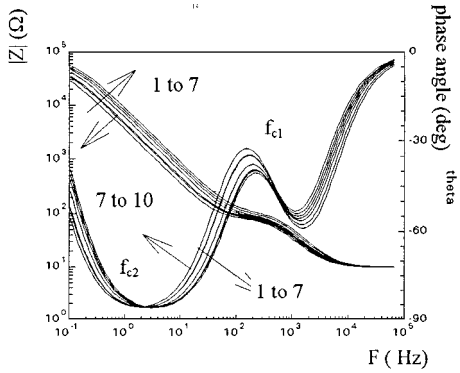

Figure 15 Experimental Bode spectra in presence of Cl^- and NO_3^- in passivity. *A*: 0.2 cm^2, pH 6, 0.1 mol dm^{-3} Cl^-, 0.1 mol dm^{-3} NO_3^-, 1: −1 V, 2: −0.97 V, 3: −0.95 V, 4: −0.92 V, 5: −0.9 V, 6: −0.87 V, 7: −0.85 V, 8: −0.82 V, 9: −0.8, 10: −0.77 V/SCE, parameter values in Table II.

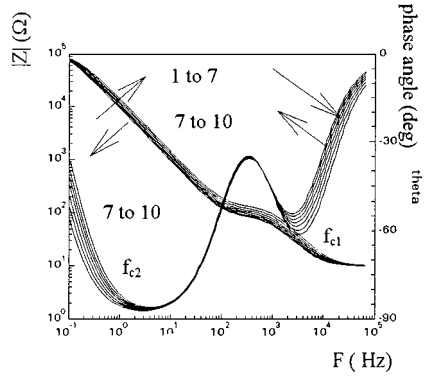

Figure 16 Experimental Bode spectra in presence of Cl^-, NO_3^- and $^3H_2O_2$ in passivity. *A*: 0.2 cm^2, pH 6, 0.1 mol dm^{-3} Cl^-, 0.1 mol dm^{-3} NO_3^-, 0.1 mol dm^{-3} $^3H_2O_2$, 1: −1 V, 2: −0.97 V, 3: −0.95 V, 4: −0.92 V, 5: −0.9 V, 6: −0.87 V, 7: −0.85 V, 8: −0.82 V, 9: −0.8, 10: −0.77 V/SCE, parameter values in Table II.

3.3. Impedance spectra

The inhibition of the chloride pitting corrosion processes is studied indirectly by the passive potentials. From this, the Bode plots for:

–Cl^- are summarized in Fig. 14,
–Cl^- and NO_3^- are given in Fig. 15,
–Cl^-, NO_3^- and $^3H_2O_2$ are given in Fig. 16.

In these figures, each Bode plot displays two main regions:

(a) At higher frequency, a dip for the characteristic frequency, f_{c_1}, in the phase angle and a linear hump of slope −1 in the impedance modulus plots which corresponds to the double layer capacitance.

(b) A second dip in the phase angle which tends to −90° at the characteristic frequency, f_{c_2} and a second linear hump of −0.9 to −1 in the impedance modulus depending on the $Cl^-/NO_3^-/^3H_2O_2$ presence which corresponds to the passive oxide layer.

3.3.1. Discussion

All the spectra have the same appearance, signifying only modification of values of discrete electrical components, which indicates that passivity is essentially dependent on the buffered pH, oxidizing power and oxide thickness. Spectra give a perfect fit with the data (Table II) if the total impedance is modeled according to the following transfer function for taking the evolutive structure into account:

$$\frac{1}{Z} = j\omega C_{\mathrm{dl}} + \frac{1}{R_{\mathrm{ct}} + \dfrac{R_{\mathrm{ox}}}{1 + (j\omega)^{\mathrm{a}} A^{-1} R_{\mathrm{ox}}}} \qquad (14)$$

where C_{dl} is the double layer capacitance, R_{ct} the charge transfer resistance, A a Constant Phase Element (CPE) replacing the oxide layer capacitance, R_{ox} the oxide resistance, ω the angular frequency and $j = \sqrt{-1}$. The transfer function given by Equation 14 includes two time constants, $\tau_1 = R_{\mathrm{ct}} C_{\mathrm{dl}}$ and $\tau_2 = R_{\mathrm{ox}}/A$ depending on the phase angle and reciprocal of the characteristic frequencies. Decreasing time constants show enhancement of oxide capacitive characteristics as indicated by Mansfield [27] and filling of metastable pits. The metastable pits must be suppressed by passivation at the early nucleation stage, and never start propagating. The greater deviation of the phase angle towards negative values as a function of the radiolytic species and passive potentials signifies that the passive layer approaches more ideal behavior.

From the data (Table II), it is interesting to note that the capacitance results for Cl^- alone reflect the poorer corrosion resistance. With NO_3^-, the oxide capacitance values indicate effective protection by adsorption of $N^3H_4^+$ and pH buffering. Also, the value of the exponent '*a*' of the CPE is close to 1 for the oxide layer obtained with NO_3^-. This value denotes the more perfect oxide layer. It can be also seen that the impedance modulus value is reduced as the spectrum passes from the passive range to the repassivation range. In this case, it should be noticed that the test, carried out in displacing the potential in the negative direction shows repassivation. These results strongly confirm that the accumulation of $N^3H_4^+$ on the Zircaloy surface enhances the oxide layer properties by blocking the chloride adsorption sites.

In presence of $^3H_2O_2$, the impedance modulus slope is slightly less than those for NO_3^- alone, thus indicating a few defects. Also, it is seen that the changing characteristic frequencies indicate a modification of the oxide

TABLE II Dependence of oxide capacitance on passive potentials for each medium

a: Results in presence of Cl^- alone

0.1 mol dm^{-3} Cl^-

E/V/SCE	−1	−0.97	−0.95	−0.92	−0.9	−0.87	−0.85	−0.82	−0.8	−0.77
C_{ox}/μF cm^{-2}	25	22	19	17	15.7	14	13	14.2	15.9	17.2

b: Results in presence of Cl^- and NO_3^-

0.1 mol dm^{-3} Cl^-, 0.1 mol dm^{-3} NO_3^-

E/V/SCE	−1	−0.97	−0.95	−0.92	−0.9	−0.87	−0.85	−0.82	−0.8	−0.77
C_{ox}/μF cm^{-2}	5	4.6	4.3	4	3.7	3.3	3	3.4	3.6	4.2

c: Results in presence of Cl^-, NO_3^- and $^3H_2O_2$

0.1 mol dm^{-3} Cl^-, 0.1 mol dm^{-3} NO_3^-, 0.1 mol dm^{-3} $^3H_2O_2$

E/V/SCE	−1	−0.97	−0.95	−0.92	−0.9	−0.87	−0.85	−0.82	−0.8	−0.77
C_{ox}/μ F cm^{-2}	2.3	2.1	2	1.8	1.6	1.5	1.3	1.6	1.7	1.9

TABLE III Dependence of oxide thickness on passive potentials for each medium

E/V/SCE	−0.95	−0.92	−0.9	−0.87	−0.85
Thickness in nm/(0.1 mol dm^{-3} Cl^-)	1	1	1.1	1.2	1.3
Thickness in nm/(0.1 mol dm^{-3} Cl^-, 0.1.mol dm^{-3} NO_3^-)	3.5	3.7	4.3	4.8	5.3
Thickness in nm/(0.1 mol dm^{-3} Cl^-, 0.1 mol dm^{-3} NO_3^-, 0.1 mol dm^{-3} $^3H_2O_2$)	8	8.9	10	10.7	12.3

layer thickness depending on the passive potentials and $^3H_2O_2$ presence, as noted by Schmuki and Böhni [28]. This fact can be associated with the nucleation of existing pits because the oxide begins to be stressed by its thickness and defects. Also, the results emphasize that the presence of $^3H_2O_2$ stimulates the repair of flawed regions of the passive layer and oxidation of the active sites on the surface. The oxide layer thus formed is more corrosion resistant. As a result a marked delay in the pitting evolution is recorded. This could be explained by reduced chloride incorporation into the oxide layer.

To ascertain the oxide layer characteristics, the thickness is obtained from the usual formula for reciprocal plane capacitance considering that r is the surface roughness factor, the vacuum permittivity ε_0 is 8.8×10^{-14} F/cm and the value of the oxide layer dielectric constant ε for ZrO_2 is about 14 [11, 15].

$$\frac{1}{C_{ox}} = \frac{d}{\varepsilon\varepsilon_0 r} \tag{15}$$

The roughness factor is calculated from measurements of profiles obtained by progressive microscopic exploration of the surface with 3D characterization [29] by Atomic Force Microscopy as shown by Marcus *et al*. [30], Farrington *et al*. [31] and Czerwinski and Szpunrr [32]. The typical surface morphology shows small semi-spherical ZrO_2 grains with 0.3 μm sides. From calculations, the root-mean-square is 150 nm and the roughness factor is 1.5. These values correspond to the results given in [33–37].

According to Table III, the oxide layer thickness grows with the passive potentials and depends on the three media: Cl^-−Cl^-/NO_3^-−$Cl^-/NO_3^-/^3H_2O_2$. From these results, it can be deduced that oxide layer thickening facilitates passivation and constraints to modify electrochemical exchange of charge across this. This means that the electrical field changes modify the carrier number and vacancies diffusion through the oxide layer. Finally, the approach of describing the oxide layer in terms of barrier properties using the Mott-Schotky equation should be valid to calculate the donor concentration as shown by Schmuki *et al*. [38].

$$n_d = \frac{2C_{ox}^2}{e\varepsilon\varepsilon_0 r}\left(V_m - V_{fb} - \frac{kT}{e}\right) \tag{16}$$

In Equation 16, V_m, V_{fb} are the potentials at which the impedance measurements are carried out and the flatband potential, respectively. Using this equation, the donor density, n_d, varies from 20 to 2 $\times$ 10^{19} carrier cm^{-3} (Table IV) signifying protection of the Zircaloy-4 by NO_3^- or $^3H_2O_2$. The higher carrier concentration for the oxide layer obtained for Cl^- alone signifies chloride diffusion. It can be also seen that n_d is lower with $^3H_2O_2$ present, indicating oxide layer thickening as reported by Di Quarto *et al*. [39]. Also, the influence of surface pH on the oxide properties should be considered through its effect on the overall oxide charge density as

TABLE IV Donor concentration and flatband potential as a function of Cl^-, NO_3^- and $^3H_2O_2$ present

Aqueous medium	Cl^-	Cl^-, NO_3^-	Cl^-, NO_3^-, $^3H_2O_2$
n_d (number of carriers per $cm^3 \times 10^{-19}$)	20	10	2
V_{fb}/V/SCE	−0.88	−0.95	−0.91

shown by Quarto *et al*. [40] and Horvat-Radosevic and Kvastek [41].

$$V_{fb} = -k - 0.06\,pH_{surface} \tag{17}$$

The flatband extrapolated potential V_{fb} is close to −0.9 V/SCE in presence of Cl^- and increases toward negative values with NO_3^- present indicating that the surface pH is buffered by $N^3H_4^+$ formation.

It is important to emphasize the role of NO_3^- and $^3H_2O_2$ in the corrosion inhibition process and to understand the interaction of these radiolytic species with the incorporated chloride throughout the layer thickness. Strehblow [42], emphasizes that the formation of a thin metal-chloride layer was observed between the oxide and the alloy. Since chloride is responsible for the formation of this inner chloride layer, this location leads to the simple conclusion that the incorporated chlorides migrate at a significantly higher rate than that of oxygen ions into oxide. This conclusion, however, leads to the following question. Is the migration of chlorides independent of, or coupled to nitrate and tritiated hydrogen peroxide concentration? We shall try to answer this question by finding a relationship between the corresponding different parameters, i.e., vacancies diffusion, pitting potential and donor density with the Cl^-, NO_3^- and $^3H_2O_2$ present.

We first propose a succession of chemical and electrochemical reactions in ZrO_2 and at its interfaces without initially taking account of Cl^-. After an adsorption stage, there is oxygen ion diffusive penetration in the oxide layer by vacancies towards the Zr–ZrO_2 interface. This can be described in the following form, as shown by Macdonald *et al*. [43] and Lorenz *et al*. [44]. Thus for this, the model contains these basic features:

—the oxide layer contains vacancies (V_{Zr}^{4+} and V_O^{2-}),
—the vacancies are in equilibrium with the aqueous media-oxide and ZrO_2–Zr interfaces,
—the passive oxide layer kinetics are governed by vacancies.

The vacancies are the limiting parameter for any diffusion. Based on these considerations, the following simplified reactions with NO_3^- alone (Equation 18) or with $^3H_2O_2$ (Equation 19) are in equilibrium at each interface:

$\{oxide^{4+}\}$ represents Zr ions in the passive oxide layer which are in equilibrium with the corresponding vacancies. In this mechanism, the electron flux in ZrO_2 is in the tritiated water direction for oxide growth. It can be seen that O^3H^- imply that the surface pH is buffered by NO_3^- which avoids local acidification according to $N^3H_4^+$ formation. Apparently, $V_{O^{2-}}$ are produced at the ZrO_2–Zr interface and consumed at the oxide-aqueous interfaces. As a result, $V_{O^{2-}}$ diffuses from the ZrO_2–Zr to the ZrO_2-aqueous interfaces. The net results of $V_{O^{2-}}$ migration can be seen by combining Equations 18,19 and 22. From the set of previous reactions, it is clear that the diffusion of $V_{O^{2-}}$ effectively results in oxide growth, should depend on flatband potential, and is produced with consumption of $^3H_2O/^3H_2O_2$ at the ZrO_2-aqueous interface where the pH is buffered throughout, whereas $\{oxide^{4+}\}$ keeps the pH buffered with $N^3H_4^+$ and O^3H^- formed as seen in Equations 7, 8, 20.

These reactions occurring on passive oxide are influenced by the different potential drops $\Delta\phi_V$ in the Zr–ZrO_2 and the ZrO_2-aqueous interfaces. Within the passive layer of a few nanometers (Table III), the potential drop into oxide is the order of some hundreds of mV [42], which enables the migration of electrons through the oxide layer at a measurable level in currents of a few μA (Fig. 1). The corresponding physical model to interpret the diffusion processes and the potential drops is shown schematically in Fig. 17. Since the ZrO_2-aqueous interface is polarizable, it is expected that the total potential drop is given by:

$$\partial\Delta E = \partial\Delta E_{ZrO_2-Zr} + 2.3\frac{kT}{2e} \times\left[\partial\log\left[NO_3^-, O^3H^-, {}^3H_2O_2\right]\right] + \partial\Delta\phi_V \tag{24}$$

where ΔE represents the potential drops between the interfaces and within the oxide layer. It is expected that:

$$\partial\left(C_{ox}^{-1}\right) = \partial\Delta E - 2.3\frac{kT}{2e}\left[\partial\log\left(NO_3^-, O^3H^-, {}^3H_2O_2\right)\right] \tag{25}$$

The oxide thickness is given by:

$$\partial d = b\left(\partial\Delta E - 2.3\frac{kT}{2e}\left[\partial\log\left(NO_3^-, O^3H^-, {}^3H_2O_2\right)\right]\right) \tag{26}$$

where b is a constant resulting from considering the oxide layer as a plane capacitor (Equation 15).

$$2V_{O^{2-}} + NO_3^- + 2\,{}^3H_2O + 8e^- \leftrightarrow \{N^3H_4^+, O^3H^-\}_{local\,pH} + 4O^{2-}\Big\} \quad \text{aqueous-}ZrO_2\text{ interface} \tag{18}$$

$$V_{O^{2-}} + 2\,{}^3H_2O_2 + NO_3^- + 12e^- \leftrightarrow \{N^3H_4^+, O^3H^-\}_{local\,pH} + 6O^{2-}\Big\} \quad \text{aqueous-}ZrO_2\text{ interface} \tag{19}$$

$$\{oxide^{4+}\} + 2\,{}^3H_2O_2 + 4e^- \leftrightarrow V_{Zr^{4+}} + ZrO_2 + 2\,{}^3H_2O\Big\} \quad \text{aqueous-}ZrO_2\text{ interface} \tag{20}$$

$$(O^3H^-)_{local\,pH}, O^{2-} + V_{O^{2-}} \leftrightarrow V_{O^{2-}} + O^{2-}\Big\} \quad \text{diffusion in } ZrO_2 \tag{21}$$

$$\left.\begin{aligned} Zr &\leftrightarrow \{oxide^{4+}\} + 2V_{O^{2-}} + 4e^- \\ Zr + V_{Zr^{4+}} &\leftrightarrow \{oxide^{4+}\} + 4e^- \end{aligned}\right\} \quad Zr-ZrO_2\text{ interface} \tag{22, 23}$$

Thus Equations 24–26 represent the functional dependence of the passive layer growth law on $\partial \Delta E$ and $\partial \log(NO_3^-, {}^3H_2O_2)$ up to a determined size also aided by the buffered pH. Therefore the formation of the oxide layer, thickness and its mode of growth are dependent on radiolytic species in tritiated water.

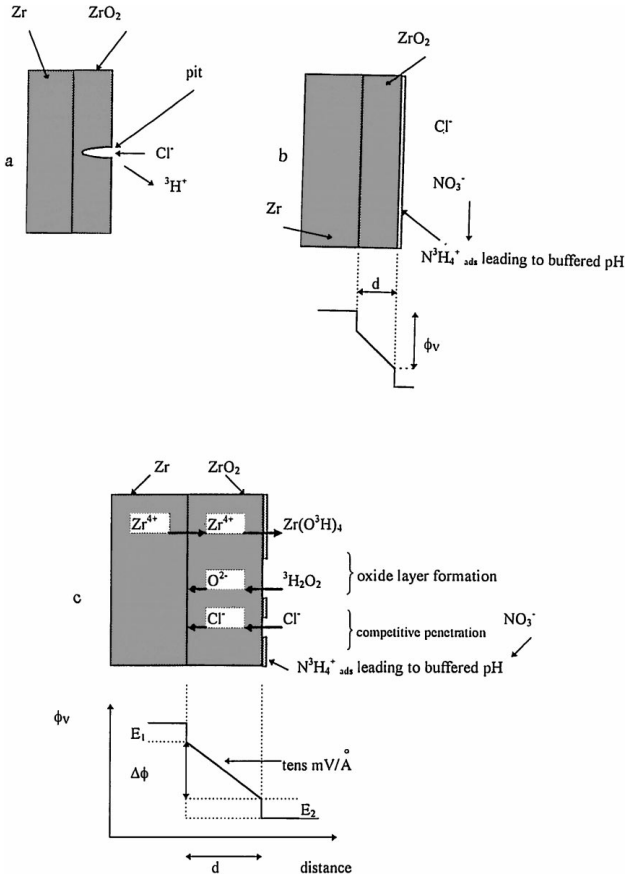

Figure 17 Physical model proposed to interpret the processes in oxide with chloride, nitrate and hydrogen peroxide, a: Cl^-, b: Cl^- and NO_3^-, c: Cl^-, NO_3^- and ${}^3H_2O_2$ present.

In presence of Cl^-, for a metastable pit at a given potential, there must be a relationship between Cl^-, NO_3^-, O^3H^- and ${}^3H_2O_2$ concentrations where the pit can be deactivated or activated. According to Strehblow [42] and Macdonald [45, 46], if the Zr vacancies penetrate the zircaloy at a slower rate than their diffusion through the oxide layer, they accumulate at the Zr–ZrO_2 interface and finally lead to a local concentration and hence will form a void. When the void grows to a certain critical size, the passive oxide layer suffers local collapse, which then marks the end of the pit incubation period. The collapsed site dissolves much faster than any other location on the layer thereby leading to pit growth. From this, the Zr vacancies are affected by the incorporation of Cl^- ions at the ZrO_2-aqueous interface as shown in the physical model (Fig. 17) and in the following equations:

$$V_{Zr^{4+}} - 2V_{O^{2-}} = 0 \tag{27}$$

$$C_{V_{Zr^{4+}}} = k\left(C_{V_{O^{2-}}}\right)^{-2} \tag{28}$$

$$V_{O^{2-}} + Cl^-_{aqueous} \leftrightarrow \{Cl^-\} \tag{29}$$

In Equations 28 and 29, $\{Cl^-\}$ is a chloride occupying O^{2-} vacancies and C the vacancies concentrations with an inverse dependence on $V_{Zr^{4+}}$ and $V_{O^{2-}}$. It can be seen from all the previous equations, that the number of $V_{O^{2-}}$ increases by introducing more NO_3^- and ${}^3H_2O_2$ and inversely decreases with $\{Cl^-\}$. Due to interdependence of the concentration of Zr and O^{2-} vacancies and the penetration of Cl^- within the oxide layer as shown by ellipsometry [47], the number of Zr vacancies decreases in the oxide layer by the presence of NO_3^- or ${}^3H_2O_2$ avoiding the critical concentration whose repercussions are shown in Figs 3, 4 and 7. From these considerations, the criterion for pit initiation in presence of NO_3^- and ${}^3H_2O_2$ can be expressed by:

$$\frac{\partial V_{Zr^{4+}}}{\partial t} = J_0\left[C_{V_{O^{2-}}}\left\{ZrO_2 - NO_3^-, {}^3H_2O_2\right\}\right]^{-2} \tag{30}$$

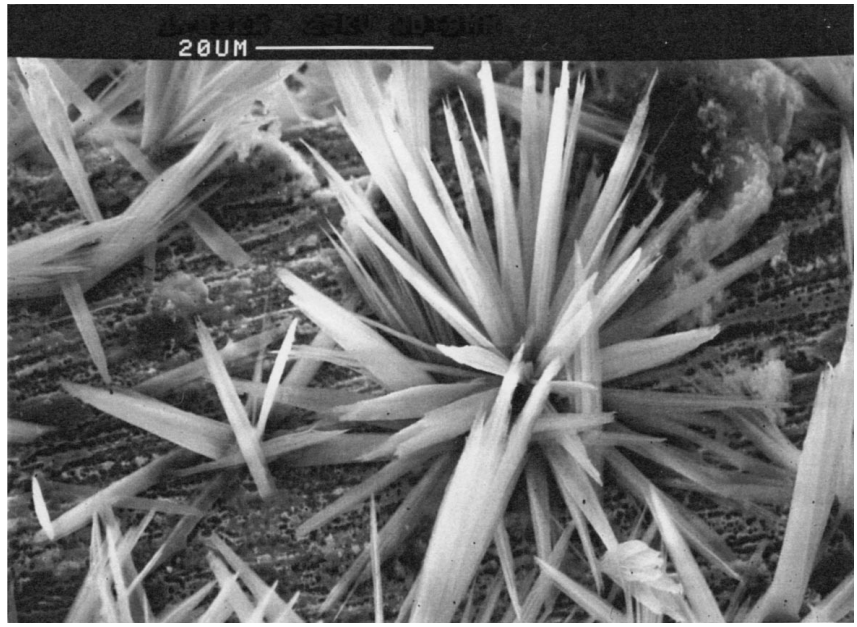

Figure 18 Scanning Electron Micrography showing repassivated pits obtained with Cl^-, NO_3^- and ${}^3H_2O_2$ and covered with zirconium oxide crystals.

where J_0 depends on thermodynamic constants and $C_{V_{O^{2-}}}\{ZrO_2-NO_3^-, {}^3H_2O_2\}$ is the concentration of O^{2-} vacancies at the ZrO_2-aqueous interface. From Equations 27–30, and applying a calculation procedure similar to that given by Strenblow [42] and Macdonald *et al.* [45, 46], we can write the simplified equation in presence of NO_3^- and ${}^3H_2O_2$:

$$E_{pit} = \frac{4.6kT}{\alpha ne}\log\left(\frac{J_m}{J_0\frac{M}{\rho}\exp\left\{\frac{(\{{}^3H_2O_2\}\{O^3H^-, NO_3^-\})}{RT}\right\}^{-0.5n}}\right) - \frac{2.3kT}{\alpha e}\log Cl^- \quad (31)$$

where J_m is the rate of submergence of the Zr vacancies in the Zircaloy-4, M the oxide molecular weight and ρ the oxide density. It can be effectively seen that higher concentrations of NO_3^-, O^3H^- and ${}^3H_2O_2$ would delay and avoid pitting by Cl^-, shifting this potential in the positive direction. This analysis should include examinations of the Zircaloy-4 surface to check the results. The absence of marked or localized corrosion in presence of NO_3^-, Cl^- and ${}^3H_2O_2$, was observed by scanning electron microscopy (Fig. 18). Only a few observable crystals covering the repassivated pits were noted. They correspond to early stage pitting.

4. Conclusions

From the experimental results, several conclusions naturally arise. The more beneficial effect is due to the radiolytic nitrate presence leading to formation of $N^3H_4^+$ and its adsorption. $N^3H_4^+$ may be considered as a counter-ion for neutralizing acid pH in the pitting process. In this connection, it is of interest to speculate that the pH is buffered on the surface oxide layer and plays a determinant role in avoiding pitting and favoring repassivation. In this case, nucleation pits do not have the possibility of being transformed to metastable or stable pits. Nitrate without hydrogen peroxide shows the greatest effectiveness against pitting corrosion. The addition of ${}^3H_2O_2$ to tritiated water containing Cl^- and NO_3^- significantly increases the thickness and changes the oxide layer characteristics. Results indicate the formation of a more stressed passive oxide than for NO_3^- alone. The pitting potential shifts towards more positive values meaning stopping of pitting formation. In contrast, the repassivation potentials shift slightly towards more negative values meaning limitation of propagation of existing pits. It is deduced that existing pits are less easily passivated with ${}^3H_2O_2$, than with NO_3^- alone. However, the two combined effects, i.e., the effects due to NO_3^- and ${}^3H_2O_2$ show greater resistance to pitting corrosion than for Cl^- alone.

References

1. G. BELLANGER, *Fusion Technology* **27** (1995) 46.
2. *Idem., J. Nucl. Mat.* **226** (1995) 104.
3. G. BELLANGER and J. J. RAMEAU, *Corros. Sci.* **39** (1997) 209.
4. G. BELLANGER, *J. Nucl. Mat.* **240** (1997) 83.
5. G. BELLANGER and J. J. RAMEAU, *Electrochim. Acta* **15** (1995) 2519.
6. *Idem., J. Mat. Sc.* **32** (1997) 4355.
7. E. BEDNARKIEWICZ and Z. KUBLIK, *Electrochim. Acta* **24** (1979) 121.
8. A. BRUGGEMAN, M. SNYKERS and P. DE REGGE, *Fusion Technology* **14** (1988) 828.
9. W. G. BURNS and P. B. MOORE, *Radiation Effects* **30** (1976) 233.
10. J. WRIGHT, J. K. LINACRE, W. R. MARSH and T. H. BATES, in Proc. Int. Conf. on the Peaceful Uses of Atomic Energy, United Nations, New York, 1956, Vol. 7, p. 560.
11. C. BATAILLON and S. BRUNET, *Electrochim. Acta* **39** (1994) 455.
12. C. LEMAIGNAN, *J. Nucl. Mat.* **187** (1992) 122.
13. E. M. PATRITO, R. M. TORRESI, E. P. M. LEIVA and V. A. MACAGNO, *Electrochim. Acta* **37** (1992) 281.
14. H. GÖHR, J. SCHALLER and C.-A. SCHILLER, *ibid.* **38** (1993) 1961.
15. G. PINARD LEGRY, "Le Zirconium," edited by G. Beranger, P. Lacombe and R. Tricot, Société Française de Métallurgie et de Matériaux-les Editions de Physique, Les Ulis, 1992) p. 35.
16. J. P. DIARD, P. LANDAUD, B. LE GORREC and C. MONTELLA, in "Deuxième Forum sur les Impédances Electrochimiques," Montrouge, 1987, edited by C. Gabrielli (University P. M. Curie, Paris, 1987).
17. J. P. DIARD, B. LE GORREC and S. MAXIMOVITCH, *Electrochim. Acta* **35** (1990) 1099.
18. M. POURBAIX, "Atlas of Electrochemical Equilibria in Aqueous Solutions," (NACE, Houston, 1974).
19. P. E. MORRIS and R. C. SCARBERRY, *Corrosion* **26** (1970) 169.
20. K. DAROWICKI and S. KRAKOWIAK, *Electrochim. Acta* **42** (1992) 2559.
21. C. R. CLAYTON, I. OLEFJORD, in "Corrosion Mechanisms in Theory and Practice," edited by. P. Marcus and J. Oudar (M. Dekler, New York, 1995).
22. I. OLEFJORD, P. FALKENBERG, L. WEGRELIUS and A. VELON, in Conf. EUROCORR' 96, Session on mechanisms of localized corrosion, OR20, Nice, September 24–26, 1996.
23. E. FUJIOKA, H. NISHIHARA and K. ARAMAKI, *Corros. Sci.* **35** (1996) 1915.
24. W. A. BADAWY and F. M. AL-KHARAFI, *ibid.* **39** (1997) 681.
25. MING-YU CHANG and GE-PING YU, *J. Nucl. Mat.* **202** (1993) 145.
26. S. A. M. REFAEY and S. S. ABG EL REHIM, *Electrochim. Acta* **42** (1997) 667.
27. F. MANSFIELD, *ibid.* **38** (1993) 1891.
28. P. SCHMUKI and H. BÖHNI, *ibid.* **40** (1995) 775.
29. A. MICHEL, "Caractérisation et mesure des microgéométries de surface," R1230 1-19, Mesures et contrôle, II (Les Techniques de l'Ingénieur, Paris, 1960).
30. V. MAURICE, W. P. YANG and P. MARCUS, *J. Electrochem. Soc.* **143** (1996) 1182.
31. K. KOWAL, J. DE LUCCIA, J. Y. JOSEFOWICZ, C. LAIRD and G. C. FARRINGTON, *ibid.* **143** (1996) 2471.
32. F. CZERWINSKI and J. A. SZPUNAR, *Corros. Sci.* **39** (1997) 147.
33. J. W. SCHULTZE and V. A. MACAGNO, *Electrochim. Acta* **31** (1986) 355.
34. L. YOUNG, "Anodic Oxide Films" (Academic Press, London, 1961).
35. O. KERREC, D. DEVILLIERS, C. HINNEN and P. MARCUS, in Symp. Modifications of Passive Films, 1993, edited by P. Marcus, B. Barouk and M. Keddam (European Federation of Corrosion, London, 1994).
36. M. J. ESPLANDIU, E. M. PATRITO and V. A. MACAGNO, *Electrochim. Acta* **40** (1995) 809.
37. W. WILHELMSEN, *ibid.* **33** (1988) 63.
38. P. SCHMUKI, M. BEUCHLER, H. BOEHNI, R. MILLER and L. J. GAUCKLER, in Proceedings of 186th Meeting Electrochem. Soc., 1994, Miami Beach, Session VII: Oxide Films on Metals and Alloys, *J. Electrochem. Soc.* **141** (1994) 362.

39. F. D. QUARTO, V. O. AIMIUWU, S. PIAZZA and C. SUNSERI, *Electrochim. Acta* **36** (1991) 1817.
40. F. D. QUARTO, S. PIAZZA, M. YANG, C. SUNSERI and S-M. CAI, *ibid.* **41** (1996) 2511.
41. V. HORVAT-RADOŠSEVIC and K. KVASTEK, *ibid.* **42** (1997) 1403.
42. H. H. STREHBLOW, in "Corrosion Mechanisms in Theory and Practice," edited by P. Marcus and J. Oudar (M. Dekker, New York, 1995) p. 201.
43. C. Y. CHAO, L. F. LIN and D. D. MACDONALD, *J. Electrochem. Soc.* **128** (1981) 1194.
44. J. B. BESSONE, D. R. SALINAS, C. E. MAYER, M. EBERT and W. J. LORENZ, *Electrochim. Acta* **37** (1992) 2283.
45. E. SIKOLA, J. SIKOLA and D. D. MACDONALD, *ibid.* **41** (1996) 783.
46. J. R. MACDONALD, "Impedance Spectroscopy" (J. Wiley, New York, 1987)
47. C. L. MCBEE and J. KRUGER "Localized Corrosion," edited by R. W. Staehle, B. F. Brown, J. Kruger, A. Agrawal (NACE, Houston, 1974) p. 252.

Received 8 January 1998
and accepted 24 August 1999